

Anomalies in the magnetoreflexion spectrum of bismuth in the low-quantum-number limit*†

M. P. Vecchi,^{‡§} J. R. Pereira,^{||} and M. S. Dresselhaus[§]

*Department of Electrical Engineering and Computer Science and Center for Materials Science and Engineering,
Massachusetts Institute of Technology, Cambridge, Massachusetts 02139*

(Received 16 March 1976)

We report here anomalies observed at high magnetic fields in the magnetoreflexion line shape of bismuth (\vec{H} parallel to binary, bisectrix axes) and bismuth-antimony alloys (\vec{H} parallel to binary axis) and associated with Landau-level transitions originating from the lowest-quantum-number ($j = 0$) levels of the valence and conduction bands. Also reported are the corresponding Shubnikov-de Haas measurements made in steady magnetic fields up to 220 kG. To interpret these anomalous magnetoreflexion line shapes an accurate model for the dispersion relations of the two coupled $j = 0$ magnetic energy levels is developed, including the dependence of the magnetic energy levels on the magnetic field and on the wave-vector component parallel to \vec{H} . This model is applied to the interpretation of the Shubnikov-de Haas data and to a magnetoreflexion line-shape calculation for the experimental conditions under which these anomalies are observed. The calculated line shapes successfully reproduce the large variety of observed line-shape anomalies as well as their relative intensities, thereby providing strong support for this description of the dispersion relations for the $j = 0$ magnetic energy levels.

I. INTRODUCTION

The present work was motivated by the previous observation of anomalies in the magnetoreflexion spectrum of bismuth.¹ These anomalies were identified with Landau-level transitions originating from the lowest-quantum-number $j = 0$ magnetic energy levels for the valence and conduction bands at the L point in the Brillouin zone, where the electron pockets for bismuth are located. The quantum number j classifies the electron Landau levels and is related to the harmonic oscillator and spin quantum numbers n and s , respectively, by

$$j = n + \frac{1}{2} - s, \quad (1)$$

where $n = 0, 1, 2, \dots$ and $s = \pm \frac{1}{2}$. The anomalies observed in the magnetoreflexion spectrum were attributed to a coupling between these $j = 0$ levels, and this coupling could not be explained on the basis of the two-band model commonly used to describe the L -point conduction and valence bands.²⁻⁵ This coupling between the two $j = 0$ levels is observed to become important when the magnetic energy-level spacing is large compared with the energy gap E_g separating the L -point valence and conduction bands.

The previous magnetoreflexion results were significant in providing the first experimental evidence in support of a magnetic field-dependent coupling effect between the two $j = 0$ levels in bismuth.¹ Such an effect had already been predicted by Baraff.⁶ The strong H dependence of this coupling provided motivation for extending the previous measurements to higher magnetic fields. These earlier measurements were made for $H \leq 70$ kG,

which will be defined in this paper as the low-field regime. Our objective was to make measurements up to higher magnetic fields in order to study quantitatively the details of this coupling effect and to investigate possible new phenomena which were expected to occur in the high-magnetic-field regime.

We report here such magnetoreflexion measurements carried out in the magnetic field range $H \leq 150$ kG. These magnetoreflexion spectra show a variety of anomalous features and provide very detailed information about the coupling process between the two $j = 0$ levels. To explain these anomalous features in detail, we have developed a quantitative model for the k_3 and H dependences of the $j = 0$ levels (k_3 being the crystal wave vector along the magnetic field direction). Furthermore, the form of this model has promise for application to bismuth-antimony alloys of low antimony concentration. The possibility of a magnetic-field-induced semimetal-semiconductor transition in bismuth and bismuth-antimony alloys⁷⁻⁹ has also stimulated interest in the magnetic field dependence of the two L -point $j = 0$ levels, which should play an important role in such a transition.

The present magnetoreflexion experiments^{10,11} were carried out using a tunable optical system in the Faraday geometry. A global light source was used in conjunction with a grating monochromator to provide a continuously tunable output between 4 and 20 μm .¹² A Bitter solenoid provided magnetic fields up to 150 kG. The sample was mounted with Be-Cu springs inside a liquid-helium cryostat using a cold-finger geometry and the sample temperature was measured by mounting a suitable

thermocouple on the optical face of the sample. The bismuth samples used in this work were prepared from single crystals which had been grown by pulling from the melt.¹³ The samples were oriented to about 2° of the specified orientation by x-ray techniques and were cut to size by a string saw (~10 × 10 × 2 mm, with the largest surface chosen as the optical face). The optical face was lapped to an optical flat and then mechanically polished, starting with 0.5-μm alumina grit, and then with finer grits down to a size of 0.05 μm. The optical surface thus obtained proved to be a good flat mirror, and the experimental magnetoreflexion traces demonstrate that no detrimental surface damage resulted from this sample preparation procedure. The same procedure described above was used for the preparation of the optical surfaces of the bismuth-antimony alloy samples.¹⁴

To provide additional support for the model developed for the $j=0$ magnetic energy levels on the basis of magnetoreflexion experiments, Shubnikov-de Haas measurements were carried out at 4.2 K in bismuth for the magnetic field orientations \vec{H} parallel to the binary axis and \vec{H} parallel to the bisectrix axis as well as in Bi_{1-x}Sb_x alloys for \vec{H} parallel to the binary axis. These measurements were made in a steady magnetic field up to 220 kG which was provided by a Bitter solenoid. In order to improve the experimental sensitivity, the magnetic field was modulated at ~10 Hz so that both the transverse H -dependent resistivity and its first derivative with respect to H could be measured.

In Sec. II we present the theoretical model that has been used to interpret the anomalous magnetoreflexion spectra which are illustrated in Sec. III and are attributed to Landau-level transitions originating from the $j=0$ levels. In Sec. IV we present the results of a magnetoreflexion line-shape calculation based on the theoretical model given in Sec. II. This model is shown to provide a detailed interpretation for the experimental data in Sec. III. Section V relates the present magnetoreflexion study to other experimental phenomena in bismuth and in the bismuth-antimony alloy system, with particular reference to Shubnikov-de Haas phenomena at high magnetic fields. Also discussed is the magnetic field dependence of the Fermi energy and of the carrier density for the various carrier pockets.

II. THEORETICAL MODEL

To provide a detailed interpretation of the magnetoreflexion experiments, it is necessary to specify the energy dispersion relation and corresponding wave functions for the magnetic energy levels. The dispersion relation for electrons in

bismuth at the L point in the Brillouin zone has been described in terms of a two-band model and is written as a (4×4) matrix^{2,4}

$$H_0 = \begin{pmatrix} \epsilon \bar{1} & i\sqrt{\epsilon} K_\alpha \bar{\sigma}_\alpha \\ -i\sqrt{\epsilon} K_\alpha \bar{\sigma}_\alpha & -\epsilon \bar{1} \end{pmatrix}, \quad (2)$$

in which $\epsilon = \frac{1}{2}E_g$, $\bar{\sigma}_\alpha$ represents the three Pauli matrices for spin $\frac{1}{2}$, the summation is made over the three α components, and $\bar{1}$ is a (2×2) unit matrix.

In a magnetic field, the vector \vec{K} becomes an operator satisfying the relation

$$\vec{K} \times \vec{K} = i\beta^* \vec{H}, \quad (3)$$

where β^* is related to the cyclotron effective mass m_c^* by

$$\beta^* = |e| \hbar / m_c^* c, \quad (4)$$

and $\beta^* H$ is interpreted physically as the Landau-level separation in both the valence and conduction bands in the limit of low magnetic fields, $\beta^* H \ll E_g$. The cyclotron effective mass m_c^* in Eq. (4) is defined by

$$m_c^* = (\det \vec{m}^* / m_H^*)^{1/2} m^{3/2}, \quad (5)$$

in which m is the free-electron mass and the effective-mass component along the magnetic field is given by

$$m_H^* = (\hat{h} \cdot \vec{m}^* \cdot \hat{h}) m. \quad (6)$$

Here \hat{h} is a unit vector along the magnetic field and the effective-mass tensor \vec{m}^* is written in dimensionless form.

The vector \vec{K} is related to the crystal momentum operator $\hbar \vec{k}$ and the coordinate operator \vec{x} by^{4,10}

$$K_1 \pm iK_2 = (\hbar / \sqrt{m_c^*}) (\tilde{k}_1 \pm i\tilde{k}_2), \quad (7a)$$

$$K_3 = (\hbar / \sqrt{m_H^*}) k_3, \quad (7b)$$

using the definitions

$$\tilde{k}_1 = k_1 + (eH/2\hbar c) x_2, \quad (8a)$$

$$\tilde{k}_2 = k_2 - (eH/2\hbar c) x_1, \quad (8b)$$

where the magnetic field is along direction 3 and the directions 1, 2 are perpendicular to each other and to \vec{H} . We note that with this definition of the coordinate system, directions (1, 2, 3) can be related to the crystallographic axes once the magnetic field direction is specified.

The strict two-band model was modified by Baraff to include the effect of the other bands as a perturbation on the two nearly degenerate bands of the two-band model, so that

$$H_B = H_0 + H_p, \quad (9)$$

where the Baraff perturbation Hamiltonian assumes the form^{6,10}

$$H_p = \begin{pmatrix} (\vec{K} \cdot \vec{B}^c \cdot \vec{K}) \bar{1} + L_\alpha^c \bar{\sigma}_\alpha & \bar{0} \\ \bar{0} & (\vec{K} \cdot \vec{B}^v \cdot \vec{K}) \bar{1} + L_\alpha^v \bar{\sigma}_\alpha \end{pmatrix}, \quad (10)$$

in which $\bar{0}$ denotes a (2×2) null matrix and the summation is made over the three α components.

The dimensionless tensors $\vec{B}^{c,v}$ are independent of H and transform in the same way as the effective-mass tensor,¹⁵ so that

$$\vec{K} \cdot \vec{B}^{c,v} \cdot \vec{K} = b_1^{c,v} \frac{\hbar^2}{m_c^*} (\tilde{k}_1^2 + \tilde{k}_2^2) + b_3^{c,v} \frac{\hbar^2}{m_H^*} \tilde{k}_3^2, \quad (11a)$$

where

$$b_3^{c,v} = \hat{h} \cdot \vec{B}^{c,v} \cdot \hat{h}, \quad (11b)$$

$$b_1^{c,v} = (\det \vec{B}^{c,v} / b_3^{c,v})^{1/2}, \quad (11c)$$

using the notation of Eqs. (5)–(8).

The vectors $\vec{L}^{c,v}$ in Eq. (10) are linearly dependent on H , and it is convenient to define new dimensionless vectors $\vec{L}^{c,v}$ by

$$\vec{L}^{c,v} = \beta^* H \vec{L}^{c,v}. \quad (12)$$

The solution of the Baraff Hamiltonian, Eq. (9), is achieved by using perturbation theory starting from the eigenvalues and eigenvectors of the strict two-band model, Eq. (2). The remainder of this section will first discuss the solution of Eq. (2) and the selection rules for optical transitions; then the solutions of the Baraff Hamiltonian will be presented. For reasons that will be discussed below, the solutions of the $j \neq 0$ and the $j = 0$ Landau levels are treated separately.

A. Strict two-band model

The Hamiltonian H_0 for the strict two-band model can be diagonalized analytically to yield the eigenvalues^{2,4}

$$E_j^\pm(\xi) = \pm [\epsilon^2 (1 + \xi^2) + 2\epsilon j \beta^* H]^{1/2}, \quad (13)$$

in which the dimensionless wave vector along the magnetic field ξ is related to k_3 by

$$\xi = \hbar k_3 / (\epsilon m_H^*)^{1/2}, \quad (14)$$

and the quantum number j is related to the orbital and spin quantum numbers n and s by Eq. (1). Although the eigenvalues $E_j^\pm(\xi)$ do not explicitly depend on s , both quantum numbers j and s are needed to specify the state which is represented by a four-component eigenvector diagonalizing H_0 . Because of the mirror symmetry of the levels in the two-band model, there is some arbitrariness in the selection of the eigenfunctions.⁴ The particular choice of eigenfunctions used in the present calculation¹⁰ is

$$\psi_{j,s,\epsilon}^*(\vec{x}) = f_j(\xi) \begin{pmatrix} l(s) \\ -i g_j(\xi) l'(s) \end{pmatrix} \phi_{n,\epsilon}(\vec{x}) \quad (15a)$$

for the conduction band; and

$$\psi_{j,s,\epsilon}^*(\vec{x}) = f_j(\xi) \begin{pmatrix} -i g_j(\xi) l'(s) \\ l(s) \end{pmatrix} \phi_{n,\epsilon}(\vec{x}) \quad (15b)$$

for the valence band, in which $f_j(\xi)$ and $g_j(\xi)$ are H - and ξ -dependent functions of the energy:

$$f_j(\xi) = \{ [E_j(\xi) + \epsilon] / 2E_j(\xi) \}^{1/2}, \quad (16a)$$

$$g_j(\xi) = 2\epsilon / [E_j(\xi) + \epsilon], \quad (16b)$$

and $E_j(\xi)$ denotes $|E_j^+(\xi)|$. The functions $l(s)$ are spinors or pure-spin states

$$l(\frac{1}{2}) = \begin{pmatrix} 1 \\ 0 \end{pmatrix}, \quad l(-\frac{1}{2}) = \begin{pmatrix} 0 \\ 1 \end{pmatrix}, \quad (17)$$

while the functions $l'(s)$ are pure-spin states only at $\xi = 0$. Away from the band edge, the $l'(s)$ functions form a linear combination of $l(s)$ functions, as seen by the ξ dependence of $l'(s)$

$$l'(\frac{1}{2}) = \begin{pmatrix} \frac{1}{2} \xi \\ \eta a \end{pmatrix}, \quad (18a)$$

$$l'(-\frac{1}{2}) = \begin{pmatrix} \eta a^\dagger \\ -\frac{1}{2} \xi \end{pmatrix}, \quad (18b)$$

in which the dimensionless energy function η is defined as

$$\eta^2 = \beta^* H / 2\epsilon, \quad (18c)$$

where η^2 is the ratio of the Landau-level separation in the low-magnetic-field limit to the zero-field-energy gap. Correspondingly, $(\xi/2)^2$ is the ratio of the kinetic energy along the magnetic field direction to the zero-field-energy gap. The non-vanishing components of $l'(s)$ at the band edge are proportional to the raising and lowering operators a and a^\dagger which act on the states of the effective-mass approximation $\phi_{n,\epsilon}(\vec{x})$, comprising the usual product of harmonics oscillator and plane-wave functions.⁴

In the presence of an electromagnetic radiation field, electric dipole transitions are induced by the coupling of the magnetic energy levels through the effective-mass velocity operator

$$V_\alpha = \left(\frac{\epsilon}{m_\alpha} \right)^{1/2} \begin{pmatrix} \bar{0} & i\bar{\sigma}_\alpha \\ -i\bar{\sigma}_\alpha & \bar{0} \end{pmatrix}, \quad (19)$$

in which α specifies the vector component index, and the notation of Eqs. (2) and (10) is used. If we choose $\alpha = 3$ to be directed along \vec{H} , then m_α is related to the effective-mass parameters by $m_1 = m_2 = m_c^*$, and $m_3 = m_H^*$.

Our magnetoreflexion experiment was carried out in the Faraday geometry using unpolarized light so that the appropriate component of the ve-

locity operator V_α for inducing electronic transitions is

$$V_\perp = (V_1 + V_2)/\sqrt{2}. \quad (20a)$$

Thus the (4×4) velocity matrix operator V_\perp is written

$$V_\perp = V_0 \begin{pmatrix} 0 & 0 & 0 & 1+i \\ 0 & 0 & -1+i & 0 \\ 0 & -1-i & 0 & 0 \\ 1-i & 0 & 0 & 0 \end{pmatrix}, \quad (20b)$$

where

$$V_0 = (\epsilon/2m_c^*)^{1/2}, \quad (20c)$$

and V_\perp corresponds to arbitrarily polarized radiation propagating along the applied-magnetic-field direction. Taking matrix elements of V_\perp between states specified by Eqs. (15) yields the general selection rules $\Delta j = \pm 1$. The velocity matrix elements connecting states for which $\Delta j = \pm 1$ are

$$\langle j, s, + | V_\perp | j \pm 1, s, + \rangle = (1-i) V_0 \times \left(\frac{(E_j + \epsilon)(E_{j \pm 1} - \epsilon)}{4E_j E_{j \pm 1}} \right)^{1/2}, \quad (21a)$$

$$\langle j, s, + | V_\perp | j \pm 1, -s, + \rangle = -(1-i) \xi V_0 \left(\frac{\epsilon^2 (E_{j \pm 1} - E_j)^2}{4E_j E_{j \pm 1} (E_{j \pm 1} + \epsilon)(E_j + \epsilon)} \right)^{1/2}, \quad (21b)$$

for intraband transitions; and

$$\langle j, s, - | V_\perp | j \pm 1, s, + \rangle = (1+i) \xi V_0 \times \left(\frac{\epsilon^2 (E_{j \pm 1} - \epsilon)}{4E_j E_{j \pm 1} (E_j + \epsilon)} \right)^{1/2}, \quad (21c)$$

$$\langle j, s, - | V_\perp | j \pm 1, -s, + \rangle = -(1+i) V_0 \left(\frac{(E_j + \epsilon)(E_{j \pm 1} + \epsilon)}{4E_j E_{j \pm 1}} \right)^{1/2} \times \left(1 + \frac{\epsilon^2 \xi^2}{(E_j + \epsilon)(E_{j \pm 1} + \epsilon)} \right) \quad (21d)$$

for interband transitions. In Eqs. (21) the Landau-level quantum number is specified by j , the spin quantum number by $s = \pm \frac{1}{2}$, the band index for the conduction and valence bands by $(+)$ and $(-)$, respectively, and E_j denotes $|E_j^+(\xi)|$. Since the dominant contribution to the optical conductivity occurs for $\xi \approx 0$, where the joint density of states between magnetic energy levels is singular, the matrix elements given by Eqs. (21) indicate that the selection rules on the spin quantum number are

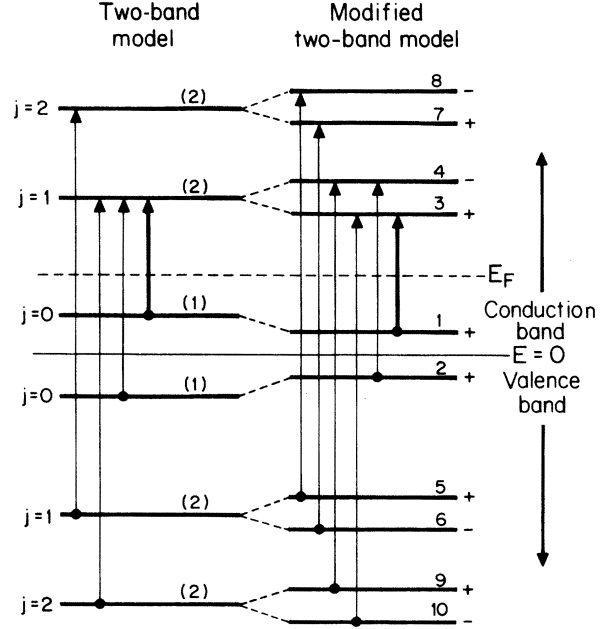


FIG. 1. Schematic representation of the magnetic energy levels of Bi for the strict two-band model (left) and the modified (Baraff) model (right). The lifting of the degeneracy of the $j \neq 0$ Landau levels is indicated, and the \pm signs to the right refer to the sign of s [see Eq. (1)]. The arrows give the allowed transitions at $k_z = 0$ in the framework of the strict two-band model (light lines denote interband transitions and heavy lines denote intraband transitions). The notation 1–6 denotes the $j=0$ and $j=1$ levels discussed in Sec. II [see Eqs. (29)], and levels 7–10 are the four $j=2$ levels.

different for intraband as opposed to interband transitions.⁴ More specifically, analysis of the strict two-band Hamiltonian yields spin-conserving intraband transitions

$$\Delta j = \pm 1, \quad \Delta s = 0 \quad (\text{intraband}), \quad (22a)$$

and spin-flipping interband transitions

$$\Delta j = \pm 1, \quad \Delta s = \pm 1 \quad (\text{interband}), \quad (22b)$$

as is indicated on Fig. 1.

To interpret the magnetoreflexion data we need to use a more sensitive model than is provided by H_0 . We will now describe how our extended model was developed using the eigenstates of H_0 as the unperturbed basis functions. This model includes both the ξ and H dependences of the eigenvalues and eigenfunctions of H_B which are necessary to carry out the magnetoreflexion line-shape calculation described in Sec. IV.

B. $j \neq 0$ Landau levels

Since these levels are doubly degenerate with energy $E_j(\xi)$ for the strict two-band model (see Fig.

1), the perturbation arising from H_p can be handled in first-order degenerate perturbation theory. For each level j of the conduction (+) and valence (-)

band, we must solve the following (2×2) secular equation, corresponding to the states $s = \pm \frac{1}{2}$ and written here for a typical level j :

$$\begin{pmatrix} \langle j, \frac{1}{2}, \pm | H_p | j, \frac{1}{2}, \pm \rangle + E_j^*(\xi) - E & \langle j, \frac{1}{2}, \pm | H_p | j, -\frac{1}{2}, \pm \rangle \\ \langle j, -\frac{1}{2}, \pm | H_p | j, \frac{1}{2}, \pm \rangle & \langle j, -\frac{1}{2}, \pm | H_p | j, -\frac{1}{2}, \pm \rangle + E_j^*(\xi) - E \end{pmatrix} = 0, \quad (23)$$

in which the notation follows that used in writing Eqs. (21). The simplicity of the magnetoreflexion spectrum observed for Landau-level transitions between $j \neq 0$ levels implies that the perturbation parameters b_1^c, v and \mathcal{L}_3^c, v ,^{5,10,15} given by Eqs. (11) and (12), are related by

$$b_1^c = -b_1^v, \quad (24a)$$

$$\mathcal{L}_3^c = -\mathcal{L}_3^v. \quad (24b)$$

The terms in Eq. (23) can then be written in a relatively simple form⁵ for both the diagonal and off-diagonal entries:

$$E_j(\xi) + \langle j, s, \pm | H_p | j, s, \pm \rangle = \pm \{ [\epsilon^2(1 + \xi^2) + 2\epsilon j\beta_B^* H]^{1/2} - 2s |G\beta^*| H \}, \quad (25a)$$

$$\langle j, s, \pm | H_p | j, -s, \pm \rangle = \pm \xi \left(\frac{E_j - \epsilon}{E_j + \epsilon} \right)^{1/2} \frac{\epsilon}{E_j} |G\beta^*| H, \quad (25b)$$

where the spin-splitting parameter G is defined by

$$G = -(b_1^c + \mathcal{L}_3^c) = (b_1^v + \mathcal{L}_3^v). \quad (26)$$

The effective-mass parameters β_B^* in Eq. (25a), rather than β^* , are measured in the magnetoreflexion experiment. We therefore redefine β^* to include the small contribution made by the perturbation Hamiltonian.⁵ In treating the various small terms (proportional to $|G\beta^*|H$) which occur in Eqs. (25), it is not necessary to distinguish between β^* and β_B^* .

The effect of the perturbation Hamiltonian is to introduce both orbital and spin corrections to the unperturbed states. The orbital corrections are mainly contained in a redefinition of β^* , while the spin correction gives rise to a splitting of each $j \neq 0$ level which is proportional to the spin-splitting parameter G . To lowest order, G is the same for each $j \neq 0$ Landau level in both the valence and conduction bands. Solution of Eqs. (23) and (25) provides both the eigenvalues and eigenfunctions for each of the spin-split levels $E_{j,s}^*(\xi)$ as a function of ξ .

The results obtained here for $\xi = 0$,

$$E_{j,s}^*(0) = \pm [(\epsilon^2 + 2\epsilon j\beta_B^* H)^{1/2} - 2s |G\beta^*| H], \quad (27a)$$

are consistent with those of Baraff for $\xi = 0$, which

is the case he considered.⁶ For the range of magnetic fields and ξ values of interest to our magnetoreflexion experiment, the off-diagonal contribution in Eq. (23) is small and the ξ dependence of $E_{j,s}^*(\xi)$ is approximately given by

$$E_{j,s}^*(\xi) \cong \pm \{ [\epsilon^2(1 + \xi^2) + 2\epsilon j\beta_B^* H]^{1/2} - 2s |G\beta^*| H \} \quad (27b)$$

as was previously given in Ref. 5. The first-order perturbation theory treatment given here for the $j \neq 0$ levels is sufficiently accurate for application to the magnetoreflexion line-shape calculation described in Sec. IV.

C. $j=0$ Landau levels

The $j=0$ levels of the valence and conduction bands are special because they are the only non-degenerate levels of the strict two-band model. Since these levels are separated by a small energy gap, which decreases as H begins to increase,¹ the separation between the two $j=0$ levels can become small compared with the Landau-level separation at high magnetic fields. In this limit we consider the two $j=0$ levels to be nearly degenerate (compared with energy separations to other levels) and the energies for these $j=0$ levels are found using degenerate perturbation theory. Thus, in this high-field regime, an interband coupling might be expected between the two $j=0$ levels. We show here that this coupling gives rise to an admixture of the wave functions for the two $j=0$ levels and that this admixture is responsible for the anomalous magnetoreflexion line shapes observed experimentally. There is no corresponding magnetic-field-induced admixture between $j \neq 0$ levels because the spin splitting and Landau-level separation each increase proportionally with increasing magnetic fields, so that no additional quasidegeneracy ever develops.

In treating the two $j=0$ levels as quasidegenerate, the lowest-order corrections are found by solving a (2×2) secular equation including terms to first-order degenerate perturbation theory. It was found that these lowest-order corrections were not accurate enough to describe the magnetoreflexion line shapes observed experimentally. A more accurate solution can be obtained in two ways: The

size of the secular equation can be increased to include other Landau levels, or alternatively, higher-order perturbation theory terms can be used in the (2×2) secular equation. Both approaches were used and the solutions obtained are consistent with each other, as will be described later. The model used for the magnetoreflexion line-shape calculations was the solution of the (2×2) secular equation because it results in a relatively simple analytical expression. Because of the great sensitivity of the anomalous magnetoreflexion line shape to the form of the $j=0$ magnetic energy levels, and because of the complexity of the line-shape calculation, it is necessary to have a very accurate but simple expression for these magnetic energy levels.

The (2×2) secular equation that was used is of the form

$$\begin{pmatrix} \mathcal{H}_{11} - E & \mathcal{H}_{12} \\ \mathcal{H}_{21} & \mathcal{H}_{22} - E \end{pmatrix} = 0. \quad (28)$$

The only nonvanishing terms of the perturbation Hamiltonian H_p are between levels for which $\Delta j = \pm 1$. Hence, the next-order correction corresponds to the coupling between the two $j=0$ levels and the four $j=1$ levels, which is treated explicitly in second-order perturbation theory. Furthermore, the mirror symmetry of the conduction and valence bands causes the contribution from the various second-order perturbation terms to nearly cancel each other. It is therefore necessary to include third-order perturbation theory terms using also the four $j=2$ levels since the second- and third-order perturbation theory terms make comparable contributions.¹⁰

Also of importance is the fact that the conduction and valence bands at $\xi=0$ have opposite parity. Hence, any perturbation due to an external magnetic field will not couple harmonic oscillator states with the same quantum numbers. Therefore, the two $j=0$ levels at $\xi=0$ will not be coupled for any order of perturbation theory. Nevertheless, the experimental magnetoreflexion results provide strong evidence that such a coupling does in fact exist at $\xi=0$, both from the magnetic field locations of the resonant structures and (as shown in Sec. IV) from the characteristics of the anomalous line shapes. In fact, the original treatment of Baraff⁶ included a nonvanishing coupling term between the two $j=0$ levels at $\xi=0$, and such a coupling term was used successfully to interpret magnetoreflexion spectra for $H < 70$ kG.¹ For these reasons, we introduce in \mathcal{H}_{12} a nonvanishing magnetic-field-dependent coupling term $Q\beta^*H$ at the band edge. A physical mechanism which could account for this coupling is the magnetic breakdown

phenomenon associated with the different geometric harmonic oscillator centers for the various band-edge states degenerate in the wave vector k_{\perp} (perpendicular to the magnetic field). These different k_{\perp} values introduce somewhat different arguments to the harmonic oscillator wave functions, thereby relaxing the harmonic oscillator selection rules. However, our main justification for the introduction of the coupling parameter Q is the excellent fit it provides for the complex experimental line shapes observed in the magnetoreflexion experiment. To yield a dispersion relation with zero slope at $\xi=0$, the parameter Q is taken as a real number.¹⁰ The coupling term $Q\beta^*H$ is of the same form as was previously introduced by Baraff.⁶ Though the magnitude of this term is small for most experimental operating conditions, it is nevertheless a crucial term in the magnetic field regime where a crossing of the $j=0$ levels would otherwise occur.

Using these arguments, the matrix elements of the (2×2) secular equation for the $j=0$ levels are given by

$$\begin{aligned} \mathcal{H}_{11} = E_0 + H_{11} + \sum_{\nu \neq 1,2} \frac{|H_{1\nu}|^2}{E_0 - E_{\nu}} \\ + \sum_{\nu, \nu' \neq 1,2} \frac{H_{1\nu} H_{\nu\nu'} H_{\nu'1}}{(E_0 - E_{\nu})(E_0 - E_{\nu'})} = -\mathcal{H}_{22} \end{aligned} \quad (29a)$$

and

$$\begin{aligned} \mathcal{H}_{12} = H_{12} + Q\beta^*H + \sum_{\nu \neq 1,2} \frac{H_{1\nu} H_{\nu 2}}{-E_{\nu}} \\ + \sum_{\nu, \nu' \neq 1,2} \frac{H_{1\nu} H_{\nu\nu'} H_{\nu'2}}{E_{\nu} E_{\nu'}} = \mathcal{H}_{21}^*, \end{aligned} \quad (29b)$$

in which $H_{l\nu}$ denotes the matrix element of H_p between states l and ν , using the eigenfunctions of Eqs. (15) and the labeling of the energy levels is given in Fig. 1. The zero-field unperturbed energy E_0 is related to

$$E_0^{\pm} = \pm \epsilon (1 + \xi^2)^{1/2}, \quad (30a)$$

with

$$E_0 = |E_0^{\pm}|. \quad (30b)$$

The unperturbed energies for the $j \neq 0$ levels, E_{ν} , are given by Eq. (13). In the off-diagonal matrix elements no distinction is made between $+E_0$ and $-E_0$ in the denominators, an approximation that is very accurate for the high- H ranges considered when $|E_{\nu}| \gg E_0$. Retaining only the leading terms in H and ξ , we obtain for the H and ξ dependences of the matrix elements of the (2×2) the explicit expressions¹⁰:

$$\begin{aligned} \mathcal{H}_{11} = & E_0 - |G\beta^*| H(1 + \xi^2)^{-1/2} \\ & - \frac{|\mathcal{L}_\perp|^2}{2} \beta^* H(1 + \xi^2)^{1/2} (1 + \xi^2/4) \\ & - \frac{|\mathcal{L}_\perp|^2 b_1}{\epsilon} (\beta^* H)^2 \end{aligned} \quad (31a)$$

and

$$\begin{aligned} \mathcal{H}_{12} = & i\xi(1 + \xi^2)^{-1/2} |G\beta^*| H + Q\beta^* H \\ & + i\xi \frac{|\mathcal{L}_\perp|^2 b_1}{2\epsilon} (\beta^* H)^2, \end{aligned} \quad (31b)$$

where the parameters $|\mathcal{L}_\perp|^2$ and b_1 are defined by the expressions

$$|\mathcal{L}_\perp|^2 = |\mathcal{L}_1^c - i\mathcal{L}_2^c|^2 = |\mathcal{L}_1^v - i\mathcal{L}_2^v|^2, \quad (32a)$$

$$b_1 = |b_1^c| = |b_1^v|. \quad (32b)$$

The resulting energy eigenvalues $E_{j=0}^\pm(\xi)$ are

$$E_{j=0}^\pm(\xi) = \pm (|\mathcal{H}_{11}|^2 + |\mathcal{H}_{12}|^2)^{1/2}. \quad (33)$$

For the special case $\xi=0$, Eq. (33) can be written in a very simple form¹⁰

$$E_{j=0}^\pm(0) = \pm [(\epsilon - |G_0\beta^*|H)^2 + (Q\beta^*H)^2]^{1/2}, \quad (34a)$$

where G_0 is defined by

$$|G_0\beta^*| = |G\beta^*| + \frac{1}{2} (|\mathcal{L}_\perp|^2) \beta^* + (|\mathcal{L}_\perp|^2 b_1/\epsilon) (\beta^*)^2 H, \quad (34b)$$

in which $|G\beta^*|$ is the spin-splitting term for the $j \neq 0$ levels.^{5,16} Values for the various parameters in Eq. (31) are found from analysis of the magneto-reflection data and are listed in Table I. The correction terms proportional to $|\mathcal{L}_\perp|^2$ and b_1 , although small, are found to be very important in the interpretation of the experimental results. In evaluating the ξ -dependent correction terms, the small differences between $|G\beta^*|$ and $|G_0\beta^*|$ are neglected.

The general features of the magnetic field dependence of the $E_{j=0}^\pm(0)$ levels shown in Fig. 2 are sensitive to the introduction of the $Q\beta^*H$ coupling term as well as to the use of higher-order corrections of the Baraff secular equation, as is clear from the form of Eqs. (34). At low magnetic fields the separation between the two $j=0$ levels decreases with increasing H , due to the term in $|G_0\beta^*|$. In the magnetic field regime where $|G_0\beta^*|H$

$\sim \epsilon$, the term $Q\beta^*H$ is important and determines the minimum-energy separation between the two $j=0$ levels. The magnetic field corresponding to this minimum-energy separation is denoted by H_{\min} . At yet higher magnetic fields, the energy separation between the two $j=0$ levels increases with increasing magnetic field and again the term in $|G_0\beta^*|H$ dominates. This behavior is illustrated in Fig. 2. From the shape of the curves in this figure, we see that there are three magnetic field regimes of interest: the low-field regime $H \ll H_{\min}$, the intermediate-field regime $H \sim H_{\min}$, and the high-field regime $H \gg H_{\min}$.

In order to test the validity of the third-order perturbation theory solutions of the (2×2) secular equation, the dispersion relations for the $j=0$ levels were also found by the alternate method of using a larger secular equation than (2×2) . Since the perturbation Hamiltonian only couples the $j=0$ levels to the $j=1$ levels, the appropriate size for the enlarged secular equation is a (6×6) , where the coupling to the $j > 1$ levels is treated in higher-order perturbation theory. The matrix elements entering the (6×6) matrix can be found using Eqs. (10) and (15), and they are given in detail in Ref. 10. The eigenvalues and eigenvectors of this (6×6) matrix are then obtained numerically.

A comparison is shown in Fig. 2 of the magnetic field dependence of the energy $E_{j=0}^\pm(0)$ as obtained from the (6×6) matrix (circles) and the (2×2) matrix (solid curve). Excellent agreement is obtained up to 200 kG, as can be seen from Fig. 2.

Excellent agreement is also found in comparing the ξ dependence of $E_{j=0}^\pm(\xi)$ as obtained from the second-order (6×6) Hamiltonian and from the third-order (2×2) Hamiltonian, as shown in Fig. 3 for the three magnetic field regimes of interest: $H \ll H_{\min}$, $H \sim H_{\min}$, and $H \gg H_{\min}$.

Of particular interest in the analysis of the anomalous magnetoreflexion line shapes is the magnetic-field-induced admixture of the eigenvectors for the $j=0$ levels. Expressing the eigenfunctions for the perturbed Landau levels $|l\rangle_p$ as a linear combination of the unperturbed eigenfunctions $|l'\rangle$,

$$|l\rangle_p = \sum_{l'} a_{ll'} |l'\rangle, \quad (35)$$

TABLE I. Numerical values for the dimensionless parameters in Eq. (31) at $T=22.5$ K.

	G	$b_1^c = -b_1^v$	$\mathcal{L}_3^c = -\mathcal{L}_3^v$	$ \mathcal{L}_\perp ^2$	$ Q $
Bi (light binary)	-7.6×10^{-3}	3.78×10^{-2}	-3.02×10^{-2}	7.7×10^{-4}	2.5×10^{-3}
Bi (light bisectrix)	-7.3×10^{-3}	2.93×10^{-2}	-2.20×10^{-2}	9.0×10^{-4}	2.4×10^{-3}
Bi (heavy bisectrix)	-8.6×10^{-3}	9.14×10^{-2}	-8.28×10^{-2}	10.7×10^{-4}	3.6×10^{-3}
Bi _{0.98} Sb _{0.02} (light binary)	-4.8×10^{-3}	1.40×10^{-2}	-0.92×10^{-2}	4.0×10^{-4}	2.0×10^{-3}

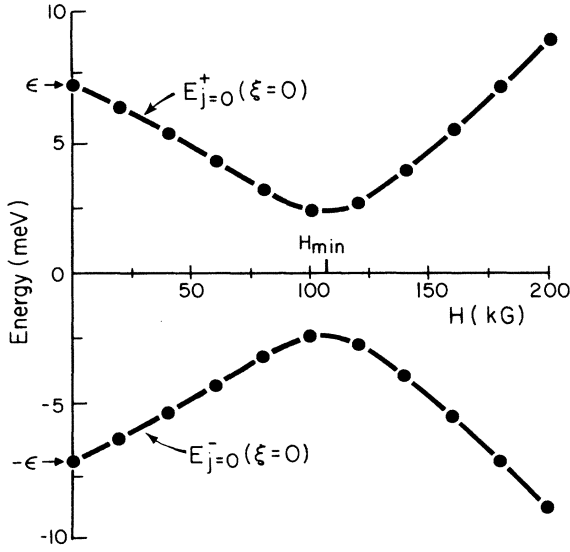


FIG. 2. Magnetic field dependence of the $j=0$ energy levels at $\xi=0$ ($k_3=0$) for the light binary electrons of Bi. The circles are the solutions to the second-order (6×6) secular equation and the solid lines are for the corresponding third-order (2×2) secular equation. The magnetic field for minimum energy separation H_{\min} is indicated and 2ϵ denotes the L -point energy gap at $H=0$.

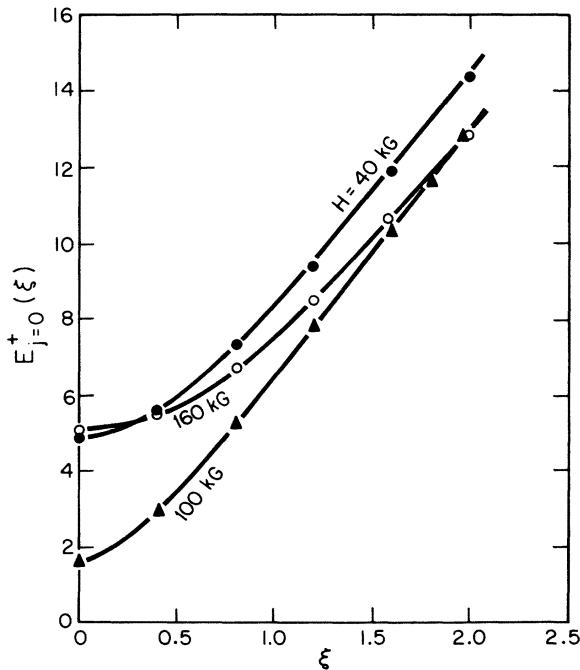


FIG. 3. Comparison between the ξ dependence of $E_{j=0}^+(\xi)$ as calculated from the third-order (2×2) secular equation (solid lines) and the second-order (6×6) secular equation (dots, crosses, and circles) for magnetic fields in the three magnetic field regimes defined in the text. $H_{\min} = 107$ kG.

we obtain coefficients a_{1l} , from the solution of the appropriate secular equation. The coefficients describing the admixture of the $j=0$ levels are a_{11} , a_{12} , a_{21} , and a_{22} , and a comparison is given here between the results from solution of the second-order (6×6) and the third-order (2×2) secular equations.¹⁷ The results for the ξ dependence of $|a_{11}|^2$ are shown in Fig. 4 where $|a_{11}|^2$ is plotted versus ξ for the three magnetic field regimes of interest. The results of Fig. 4 are significant in showing a large admixture of the unperturbed wave functions at high magnetic fields. The figure also shows that good agreement between the (6×6) and the (2×2) solutions is obtained for fields up to 160 kG, which is the magnetic field range of interest in our magnetoreflexion experiments. The large admixture of wave functions indicated in Fig. 4 is responsible for the dramatic change in magnetoreflexion line shape that is found by comparing spectra in the three pertinent magnetic field regimes.

The solution of the third-order (2×2) secular equation discussed above will be applied in the fol-

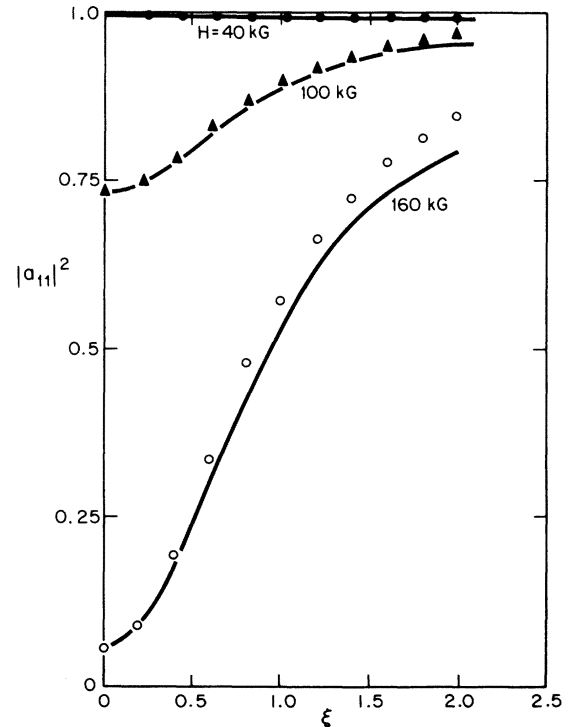


FIG. 4. Comparison between the ξ dependence of the expansion coefficient squared $|a_{11}|^2$ [see Eq. (35)], as obtained with the second-order (6×6) secular equation (dots, crosses, and circles), and with the third-order (2×2) secular equation (solid curves) for magnetic fields in the three magnetic field regimes defined in the text. $H_{\min} = 107$ kG.

lowing sections to the interpretation of magnetoreflexion and Shubnikov-de Haas experiments. It will be seen that excellent agreement is found between calculations based on this secular equation and the experimental results.

III. EXPERIMENTAL MAGNETOREFLECTION RESULTS

A sequel of typical magnetoreflexion traces is shown in Fig. 5 for \vec{H} parallel to the binary axis. At low magnetic fields, the observed resonant structures are associated with interband Landau-level transitions between valence level j_v and conduction level j_c and denoted by $j_v \rightarrow j_c$. These resonances for $j_v, j_c \neq 0$ are shown in more detail in the experimental traces of Fig. 6, taken at a photon energy of $\hbar\omega = 248.56$ meV. The same characteris-

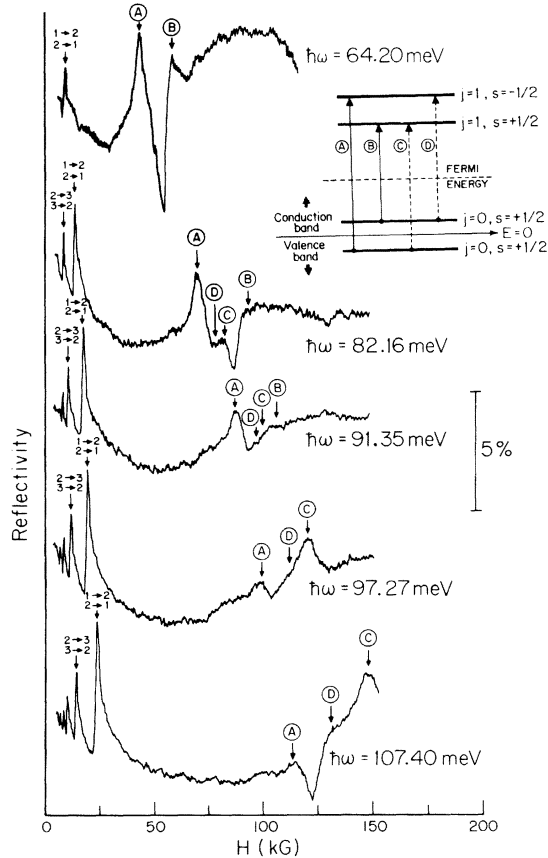


FIG. 5. Experimental magnetoreflexion traces for bismuth at $T \sim 22.5$ K for several incident photon energies and \vec{H} parallel to the binary axis. The insert defines the notation used in the traces to label the intraband and interband transitions originating from the $j = 0$ levels. The solid arrows label transitions appropriate to low magnetic fields and follow the selection rules of Eqs. (22). The dashed arrows denote optical transitions occurring at high magnetic fields due to interband coupling between the two $j = 0$ levels.

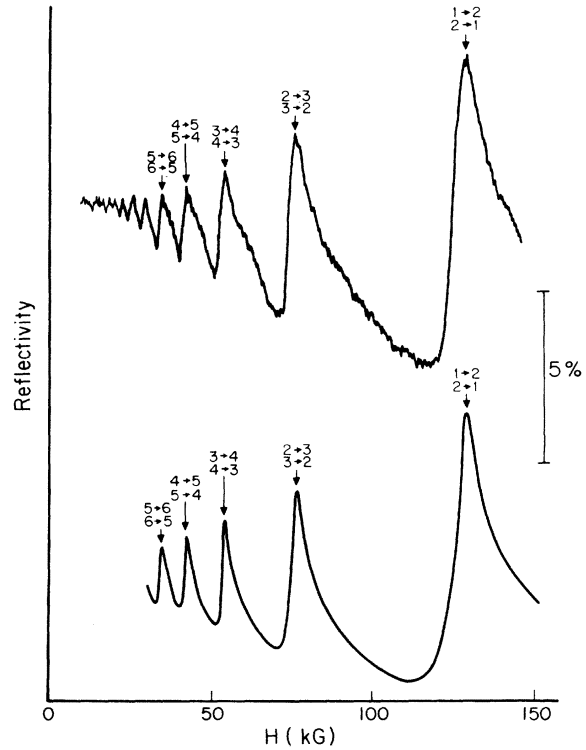


FIG. 6. Comparison between experimental (upper curve) and calculated (lower curve) magnetoreflexion line shapes for the $j \neq 0$ transitions, with $\hbar\omega = 248.58$ meV, \vec{H} parallel to the binary axis and $T \sim 22.5$ K. The resonant magnetic field for the $j_n \rightarrow j_{n+1}$ and $j_{n+1} \rightarrow j_n$ interband transitions are associated with the reflectivity maxima.

tic line shapes as are illustrated in Fig. 6 are observed over a wide range of photon energies, magnetic fields, and quantum numbers. A single resonant structure is found for each value of $j_v + j_c$. Contributions to a given $j_v + j_c$ resonance are made predominantly by the four spin-flipping transitions of equal energy in accordance with the selection rule given by Eq. (22b).

More complicated magnetoreflexion line shapes are, however, found for the various resonant transitions originating from the $j = 0$ levels which appear at higher magnetic fields. These transitions are shown in Fig. 5 for \vec{H} parallel to the binary axis and are labeled in accordance with the insert given in this figure. Both intraband and interband transitions contribute to these resonant structures, and the theoretical values for the resonant magnetic fields for the (A), (B), (C), and (D) transitions are indicated above the traces. (See Sec. IV for a discussion of the theoretical line shapes and the relative intensities of the various transitions.) In the low-magnetic-field regime ($H \ll H_{\min}$) which applies to the top trace taken at $\hbar\omega = 64.20$ meV, interband transition (A) and intra-

band transition (B) are observed in accordance with the selection rules given by Eqs. (22). Differences in the line shape for the interband transition (A), as compared with those shown in Fig. 6, are largely due to the much higher nonparabolicity of the initial $j=0$ level so that there is a large difference in curvature between the $j=0$ and $j=1$ levels near $k_3=0$. Therefore, for a given spectral width of incident radiation, interband transitions will be excited for a greater range of k_3 values in the case of the $j \neq 0$ interband transitions than for transitions (A) from the $j=0$ initial state.

In the top trace of Fig. 5, the resonant structure for the intraband transition (B) has a step-like shape, while interband transition (A) exhibits a resonant peak; these resonant structures are designated as the "normal" line shapes and have been discussed previously.^{1,3,5} These normal line shapes occur in the low-field regime where coupling between the two $j=0$ levels is relatively unimportant. On the other hand, for the trace taken at $\hbar\omega = 107.40$ meV, the transitions originating from the $j=0$ levels occur in the high-field regime ($H \gg H_{\min}$), where there is a large interband coupling between the two $j=0$ states. In this regime transitions (C) and (D) are dominant, contrary to the selection rules of Eqs. (22). The resulting line shapes are very different from the normal line shapes and are designated as "anomalous."

Referring again to Fig. 5, we see the development of the line shapes for the cluster of $j=0$ transitions as the incident photon energy is increased and the resonances move to higher magnetic fields. For $\hbar\omega = 82.16$ meV, the cluster of $j=0$ transitions occurs at $H \approx 80$ kG, and transitions (C) and (D) begin to appear, although the normal line shape is still dominant. For $\hbar\omega = 91.35$ meV, the cluster of $j=0$ transitions has moved out to $H \approx 100$ kG. Here the admixture of the $j=0$ levels has become important, and noticeable deviations from the normal line shape are observed, with all four transitions contributing significantly. As $\hbar\omega$ is further increased to 97.27 meV, the cluster of $j=0$ transitions moves out to $H \approx 120$ kG and transitions (C) and (D) become more pronounced. The observation of this sequence of anomalous magnetoreflexion line shapes provides strong evidence for the coupling between the two $j=0$ levels and the breakdown of the selection rules of the strict two-band model. In particular, we conclude that for $H \geq 120$ kG, with \vec{H} parallel to the binary axis, this coupling between the $j=0$ levels dominates the anomalous line-shape characteristics, as is shown in the trace for $\hbar\omega = 107.40$ meV.

To substantiate this interpretation, magnetoreflexion experiments were performed for \vec{H} parallel to the bisectrix axis, for which resonant magneto-

reflection transitions are observed for two sets of electron pockets: The light bisectrix electrons have a cyclotron mass somewhat smaller than that for the light binary electrons, and the heavy bisectrix electrons have a cyclotron mass considerably larger than the light binary mass. Since E_g is independent of the direction of \vec{H} , one would expect the interband coupling between the two $j=0$ levels to be larger for the light bisectrix electrons and smaller for the heavy bisectrix electrons as compared with the light binary electrons. These predictions are in agreement with the experimental observations described below.

Figure 7 shows a sequence of magnetoreflexion traces taken with \vec{H} parallel to the bisectrix axis and resonant transitions for the light and heavy bisectrix electrons are identified in the figure. At

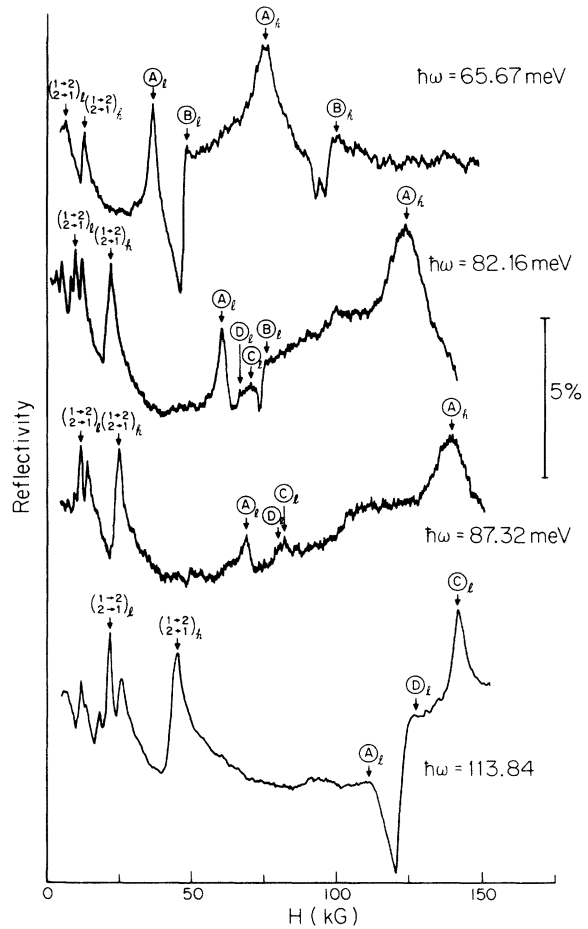


FIG. 7. Experimental magnetoreflexion traces for bismuth at $T \sim 22.5$ K for several incident photon energies and \vec{H} parallel to the bisectrix axis. The subscripts l and h refer to the light and heavy bisectrix electrons and the notation for the transitions originating from the $j=0$ levels follows the insert in Fig. 5.

higher magnetic fields, two clusters of $j=0$ transitions are found corresponding to the light and heavy bisectrix electrons and are labeled accordingly. The trace for $\hbar\omega=65.67$ meV shows the “normal” line shapes for both the light and heavy bisectrix electrons, though the resonances for the heavy bisectrix electrons occur in the 90-kG range. In fact, a normal line shape is observed for the heavy bisectrix electrons up to the maximum available field of 150 kG. On the other hand, at 70 kG the light bisectrix electrons show evidence for the existence of the transitions (C) and (D) as is seen in the traces taken for $\hbar\omega=82.16$ and 87.32 meV. The transitions at $\hbar\omega=87.32$ meV are of particular interest because all the transitions from the $j=0$ levels have approximately equal amplitudes, though the intensity for the whole resonant structure tends to be weak for $H \sim H_{\min}$. Finally, the trace at $\hbar\omega=113.84$ meV, corresponding to the $H \gg H_{\min}$ region, again shows a large intensity for the cluster of $j=0$ resonances for the light bisectrix electrons. This line shape is dominated by resonances (C)_l and (D)_l and provides clear evidence for the strong coupling between the two $j=0$ levels which breaks down the selection rules of Eqs. (22).

This interpretation of the anomalous line shape of the magnetoreflexion resonances associated with the $j=0$ levels is further substantiated by looking at the variation of the coupling between the two $j=0$ levels caused by changing the energy gap, either by alloying with Sb or by varying the temperature. For example, the relative intensities of the resonances (C) and (D) for a given magnetic field are much stronger for the $\text{Bi}_{0.98}\text{Sb}_{0.02}$ alloy ($E_g=8.0$ meV)¹⁰ than for pure bismuth ($E_g=13.8$ meV)¹, and, in fact, for \vec{H} parallel to the binary axis, the line shapes for the $j=0$ cluster of transitions for pure bismuth at $\hbar\omega=107.40$ MeV [H (resonance) ≈ 130 kG] are almost identical to those for $\text{Bi}_{0.98}\text{Sb}_{0.02}$ at $\hbar\omega=84.46$ meV [H (resonance) ≈ 80 kG].^{10,18} Our study of the BiSb alloys show that the smaller the energy gap the lower is H_{\min} , the field at which the interband mixing becomes important.¹⁰ It is furthermore found that the anomalous magnetoreflex-

ion line shapes persist as the Sb concentration is increased to produce a band crossing between the L -point valence and conduction bands.¹⁰

As the temperature is increased, the L -point energy gap for pure bismuth increases,¹⁹ the coupling between the two $j=0$ levels is expected to decrease, and the more “normal” magnetoreflexion line shapes should be favored. This prediction has in fact been confirmed by magnetoreflexion measurements in pure bismuth up to 280 K,¹⁹ and in the $\text{Bi}_{0.98}\text{Sb}_{0.02}$ alloy up to 77 K.¹⁰

By comparing the observed and calculated locations in magnetic field and photon energy of the various Landau-level transitions, values for various band parameters for pure bismuth are deduced and these are summarized in Table II. Also included in this table are parameters for the $\text{Bi}_{0.98}\text{Sb}_{0.02}$ alloy, which is well described by the same form of the dispersion relations as apply to pure bismuth.¹⁰ A detailed comparison between these results and previously published results^{5,20,21} is given in Ref. 10.

IV. MAGNETOREFLECTION LINE-SHAPE CALCULATION

The calculation of the magnetoreflexion spectrum in the “anomalous” line-shape regime provides a sensitive test for the details of the model for the $j=0$ magnetic energy level structure. In this section, we show that the band model discussed in Sec. II provides, with a single set of band parameters, a quantitative fit to the variety of line shapes observed for the cluster of resonances associated with the $j=0$ initial states in the three magnetic field regimes of interest: $H \ll H_{\min}$, $H \sim H_{\min}$, and $H \gg H_{\min}$. This model also allows a quantitative interpretation to be made for the resonances associated with the $j \neq 0$ levels, in agreement with the work of Maltz.¹⁵

The optical reflectivity is calculated using the optical conductivity tensor²²

$$\sigma_{\alpha\beta} = -e^2 \sum_{l,l'} \frac{(f_l - f_{l'}) \langle l | V_\alpha | l' \rangle \langle l' | V_\beta | l \rangle}{(E_l - E_{l'}) [(i/\hbar)(E_l - E_{l'}) - i\omega + 1/\tau]}, \quad (36)$$

TABLE II. Numerical values of band parameters for Bi and $\text{Bi}_{0.98}\text{Sb}_{0.02}$.

	E_g (meV)	$10^5 (m_c^*/m)$	$E_g\beta^*$ (meV ² /kG)
Bi (light binary, 22.5 K)	13.8	198	82.1
Bi (light bisectrix, 22.5 K)	13.8	177	92.1
Bi (heavy bisectrix, 22.5 K)	13.8	351	46.3
Bi (light binary, 84 K)	15.5	243	76.7
Bi (light bisectrix, 84 K)	15.5	219	85.3
Bi (heavy bisectrix 84 K)	15.5	137	43.3
$\text{Bi}_{0.98}\text{Sb}_{0.02}$ (light binary, 22.5 K)	8.0	116	80.1
$\text{Bi}_{0.98}\text{Sb}_{0.02}$ (light binary, 84 K)	9.0	138	78.4

where l and l' denote the full set of quantum numbers for the initial and final states, and f_i is the Fermi function at energy E_i which enters Eq. (36) because the electronic transitions occur from an occupied to an unoccupied state.²³ In a magnetic field, the full set of quantum numbers includes the band index \pm , the spin quantum number s , the Landau-level index n , and the crystal wave-vector components k_1 and k_3 which are, respectively, perpendicular and parallel to \vec{H} . The summation over states is simplified because the energies E_l and $E_{l'}$ do not depend on k_1 and because the velocity matrix elements $\langle l | V_\alpha | l' \rangle$ only couple a restricted number of states through selection rules such as given by Eqs. (22).

In the Faraday geometry, used in the present magnetoreflexion experiment, it is only the velocity matrix elements of V_\perp such as those given by Eq. (21) which contribute $\sigma_{\alpha\beta}$. Because of the resonant denominator in Eq. (36), the major contribution to the optical conductivity occurs for photon energies $\hbar\omega$ equal to the Landau-level separation at $k_3 \sim 0$ where the joint density of states is a maximum. The explicit sum over the quantum numbers (\pm, n, s) in Eq. (36) is carried out only for those states with energy differences comparable to the incident photon energy, and the sum over k_3 is performed by integration. All other transitions are nonresonant and are treated through the introduction of a background conductivity σ_b or core dielectric constant $4\pi i\sigma_b/\omega$. For the case of the L -point transitions in bismuth, the background conductivity was found to be almost purely imaginary and proportional to ω , yielding a real frequency-independent core dielectric constant.¹⁵ The zero-field background reflectivity is taken to be independent of ω for the small frequency range considered in this experiment,¹⁰ in accordance with the measurements of Nanney.²⁴ Because the experimental magnetoreflexion traces exhibit some background field dependence on which the resonant structures are superimposed, a weak magnetic field dependence is introduced in the background conductivity σ_b , such that at $H=100$ kG, σ_b is about one half of its zero-field value.¹⁰

The results of our line-shape calculations for the transitions associated with the $j \neq 0$ levels are shown in Fig. 6. A previous calculation by Maltz¹⁵ yielded good agreement with the general features of the observed resonant structures by merely using a constant core dielectric constant. It is of importance to note that the resonant magnetic fields for the four transitions, which contribute to a given resonant structure $(j_v + j_c)$, are closely equal to each other and give rise to a single sharp resonant structure. This observation is the basis for the simplification of the Baraff Hamiltonian

used in the present work.^{5,6,15}

It was noticed¹⁰ that a better fit to the observed asymmetry of the magnetoreflexion line shapes of Fig. 6 is achieved by assuming a ξ dependence [see Eq. (14)] in the relaxation time τ . In particular, the calculated line shapes shown in Fig. 6 were obtained for $\tau(\xi=0) \simeq 4 \times 10^{-13}$ sec (or $\hbar/\tau \sim 1.5$ meV), in agreement with the value used by Maltz,¹⁵ but the relaxation energy was assumed to increase with ξ^2 such that at $\xi=1$, $\hbar/\tau \sim 3$ meV. This form of the ξ dependence of the relaxation time is physically reasonable because as ξ becomes smaller, the number of available final scattering states also becomes smaller. It is of interest to point out that our value of τ is much shorter than values of τ obtained from the analysis of Shubnikov-de Haas,²⁵ far-infrared cyclotron resonance,²⁶ and transport measurements.²⁷ This shorter relaxation time at infrared frequencies is consistent with frequency-dependent relaxation processes in bismuth^{26,28} and indicates that different scattering mechanisms are important for the interband processes which dominate the magnetoreflexion experiment. Figure 6 shows that the present calculation provides a good fit to the experimental spectrum associated with the $j \neq 0$ levels, both with regard to the position of the resonances (located at the reflectivity maxima) and to their line shapes.

The observed magnetoreflexion line shapes for the cluster of resonances associated with transitions originating from the $j=0$ levels are more complex, as can be seen in the sequence of traces shown in Fig. 5. These line shapes are dependent on H and are sensitive to the magnetic-field-induced mixing of the wave functions for the two $j=0$ levels, which results in a breakdown of the selection rules of Eqs. (22). In calculating the optical conductivity for this cluster of transitions, the initial state is one of the $j=0$ levels given by the $|l\rangle_p$ representation of Eq. (35), while the final state is a $j=1$ conduction state, obtained from Eq. (23). The velocity matrix element coupling the initial state $|l\rangle_p$ to a final state $\langle l'|$ is written as $\langle l' | V_\perp | l \rangle_p$ where

$$\langle l' | V_\perp | l \rangle_p = \sum_{l''} a_{ll''} \langle l' | V_\perp | l'' \rangle, \quad (37)$$

in which $\langle l' | V_\perp | l'' \rangle$ is the velocity matrix element calculated with respect to the unperturbed states in Eq. (21). It is convenient to use the notation M_1 and M_2 , respectively, for the velocity matrix elements of the interband and intraband transitions which are allowed at $\xi=0$ by the selection rules of Eqs. (22). These matrix elements are generally defined as

$$\begin{aligned} M_1 &\equiv \langle 1, -\frac{1}{2}, + | V_{\perp} | 0, \frac{1}{2}, - \rangle, \\ M_2 &\equiv \langle 1, \frac{1}{2}, + | V_{\perp} | 0, \frac{1}{2}, + \rangle. \end{aligned} \quad (38)$$

The band-edge matrix elements M_A^0 , M_B^0 , M_C^0 , and M_D^0 (at $\xi=0$) associated with the four transitions specified by the insert in Fig. 5 are written

$$\begin{aligned} M_A^0 &= a_{22} M_1^0, \quad M_B^0 = a_{11} M_2^0, \\ M_C^0 &= a_{21} M_2^0, \quad M_D^0 = a_{12} M_1^0, \end{aligned} \quad (39)$$

in which M_1^0 and M_2^0 are found by evaluating the indicated matrix elements in Eq. (38) at $\xi=0$. At low magnetic fields, $H \ll H_{\min}$, the coefficients a_{11} and a_{22} are nearly unity (as shown in Fig. 4), and the coefficients a_{12} and a_{21} are very small, so that there is negligible admixture of the $j=0$ wave functions and the simple "normal" line shape results. On the other hand, at very high magnetic fields where $H \gg H_{\min}$, Fig. 4 shows that at $\xi \approx 0$, $|a_{12}| \gg |a_{11}|$ and $|a_{21}| \gg |a_{22}|$, so that the strict two-band model selection rules break down and transitions (C) and (D) dominate. For intermediate magnetic fields $H \sim H_{\min}$, all four coefficients $a_{i'}$ of Eq. (37) are of comparable magnitude and the resulting line shape shows contributions from all four types of transitions.

The general features of the observed line shapes can be reproduced by performing a calculation in which only the transitions M_1 and M_2 of Eq. (38) are considered. To improve the agreement between the calculated and experimental line shapes, it is necessary to include also the transitions with matrix elements M_3 (interband) and M_4 (intraband):

$$\begin{aligned} M_3 &\equiv \langle 1, \frac{1}{2}, + | V_{\perp} | 0, \frac{1}{2}, - \rangle, \\ M_4 &\equiv \langle 1, -\frac{1}{2}, + | V_{\perp} | 0, \frac{1}{2}, + \rangle, \end{aligned} \quad (40)$$

which vanish at $\xi=0$. The ξ -dependent expressions used in our calculations are obtained from Eq. (37) and are given by

$$\begin{aligned} M_A &= a_{22} M_1 + a_{21} M_4, \quad M_B = a_{11} M_2 + a_{12} M_3, \\ M_C &= a_{21} M_2 + a_{22} M_3, \quad M_D = a_{12} M_1 + a_{11} M_4. \end{aligned} \quad (41)$$

It should be pointed out that all the quantities in Eq. (41) are complex, and therefore great care must be exercised in combining their magnitudes and phases to calculate the velocity matrix elements given by Eq. (41).

In carrying out the magnetoreflexion line-shape calculation, the contributions from those transitions having energy separations comparable with the photon energy were treated in detail, while other contributions were included using a background conductivity term. Since the resonant terms in this case are especially sensitive to the contributions from the region around the magnetic subband extrema, the ξ -independent relaxation

time proved adequate for this line-shape calculation, in contrast with transitions between $j \neq 0$ levels.

The results of this line-shape calculation are shown in Figs. 8 and 9. Also included in these figures are the experimental traces corresponding to each calculated spectrum. The parameters used in this line-shape calculation are given in Tables I and II, and the values for σ_r and $\tau(\xi=0)$ are approximately the same as were used for the line shape calculated for the $j \neq 0$ transitions shown in Fig. 6.

The sequence of line shapes shown in Fig. 8 corresponds to the regime $H \lesssim H_{\min}$. The top trace taken at $\hbar\omega = 64.20$ meV shows a typical normal line shape. The line-shape calculation in this regime ($H \ll H_{\min}$) is relatively simple since only the interband transition (A) and the intraband transition (B) contribute significantly. The resonant magnetic fields for transitions (A) and (B) shown on the theoretical curve correspond to the contribution from $\xi=0$, where the singularity in the joint density of states occurs. Comparison between the calculation and the experimental trace shows that the resonant magnetic field for interband transition (A) is identified with the peak in the reflectivity, while for intraband transition (B) the identification is with the maximum in the overshoot of the step-like structure in the reflectivity. As the pho-

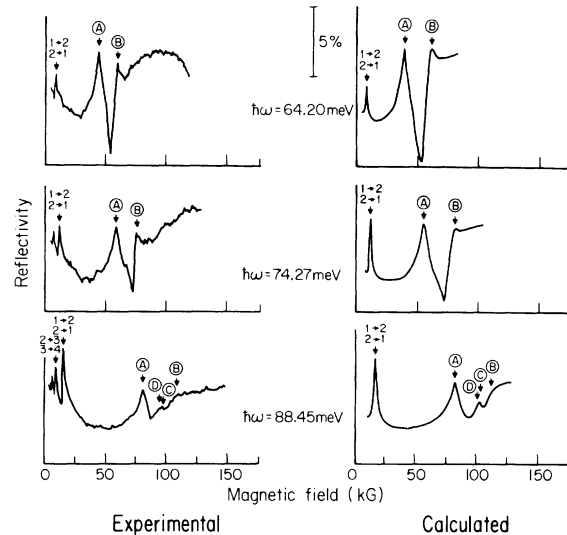


FIG. 8. Sequence of magnetoreflexion line shapes for three photon energies showing the change in line shape in going from the low-field ($H \ll H_{\min}$) to the intermediate-field ($H \sim H_{\min}$) regimes. The data are for \vec{H} parallel to the binary axis and $T \sim 22.5$ K in bismuth. The left side shows the experimental traces and the right side the calculated line shapes. The resonant transitions are labeled according to Figs. 5 and 6.

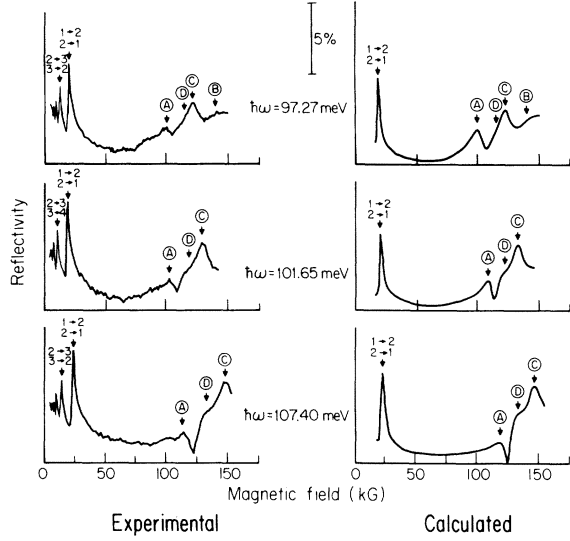


FIG. 9. Sequence of magnetoreflexion line shapes for three photon energies following the sequence shown in Fig. 8 to higher magnetic field from the $H \sim H_{\min}$ to the $H \gg H_{\min}$ regimes. The data are for \vec{H} parallel to the binary axis and $T \sim 22.5$ K in bismuth. The left side shows the experimental traces and the right side the calculated line shapes. The resonant transitions are labeled according to Figs. 5 and 6.

ton energy is increased to $\hbar\omega = 74.27$ meV, the observed decrease in intensity of transitions (A) and (B) is reproduced in the theoretical curve, and the same identification as described above is made for the resonant magnetic fields for transitions (A) and (B). This decrease in intensity is associated with the onset of interband coupling between the two $j = 0$ levels which reduces the amplitudes for the matrix elements for the (A) and (B) transitions. Of interest is the small structure observed between the (A) and (B) resonances in the experimental trace. The calculation shows this structure to be associated with contributions from the (C) and (D) transitions, which begin to contribute in this magnetic field range.

The magnitudes of the (C) and (D) transitions further increase as $\hbar\omega$ is increased to 88.45 meV, and the resonant magnetic fields move into the regime $H \approx H_{\min}$. For this photon energy, all four transitions (A), (B), (C), and (D) are of approximately the same amplitude, and the line-shape calculation is extremely sensitive to the detailed description of the dispersion relation for the $j = 0$ levels. The different phases associated with the four velocity matrix elements in Eq. (41) can make the overall intensity small, even though each individual transition makes a substantial contribution (this effect is also seen in Fig. 7 for \vec{H} parallel to the bisectrix axis). The identification of the resonant magnetic fields, which is extremely dif-

ficult in the $H \approx H_{\min}$ regime, becomes clearer as the photon energy is further increased and the resonances move to higher H .

The sequence of magnetoreflexion line shapes corresponding to this higher-field regime $H \gtrsim H_{\min}$ is shown in Fig. 9. The top trace, taken at $\hbar\omega = 97.27$ meV, already shows a strong contribution from the (C) and (D) transitions. To reproduce the experimental traces for both $\hbar\omega = 88.45$ and 97.27 meV for a single set of band parameters proved to be difficult. The further constraints imposed by also fitting the experimental traces for $H \ll H_{\min}$ and $H \gg H_{\min}$ made the magnetoreflexion line-shape calculation especially sensitive to the form of the dispersion relations for the $j = 0$ levels and the values for the band parameters. The calculated line shapes in the regime $H \sim H_{\min}$ are particularly sensitive to the coupling term QB^*H in Eq. (29b), and they provided an accurate method for the determination of the parameter Q .

As we follow the magnetoreflexion line shapes through $\hbar\omega = 101.65$ and 107.40 meV we get into the high-field regime where transitions (C) and (D) assume a dominant role. Here we see that intraband transition (C) is identified with a peak in the reflectivity and interband transition (D) with the maximum change in slope of the step-like structure characterizing this interband transition (see Fig. 9). This interchange in the line shapes for interband and intraband transitions in going from the $H \ll H_{\min}$ regime to the $H \gg H_{\min}$ regime provides strong support for the interband coupling of the two $j = 0$ levels. Our calculated line shape is successful in reproducing both the great variety of line shapes found in the experimental traces and the relative intensities of the various resonant structures.

We note that for all the traces in Fig. 9, the interband transition (C) occurs at a higher magnetic field than the intraband transition (D), which is in contrast with the normal case where interband transition (A) always occurs at lower magnetic fields than intraband transition (B). This anomalous effect arises because the spin splitting of the $j = 1$ levels is larger than the interband separation between the two $j = 0$ levels (at $\xi = 0$) in this magnetic field regime. This point is illustrated more clearly in Fig. 10 where we plot the resonant photon energies (at $\xi = 0$) for each of the four transitions versus H . Whereas transition (A) in Fig. 10 always occurs at lower H than (B), the relative ordering of (C) and (D) is more complicated, depending on the relative magnitudes of the $j = 1$ spin splitting and the separation of the $j = 0$ levels. Since the H dependence of the $j = 0$ level separation at high fields is greater than the linear H depen-

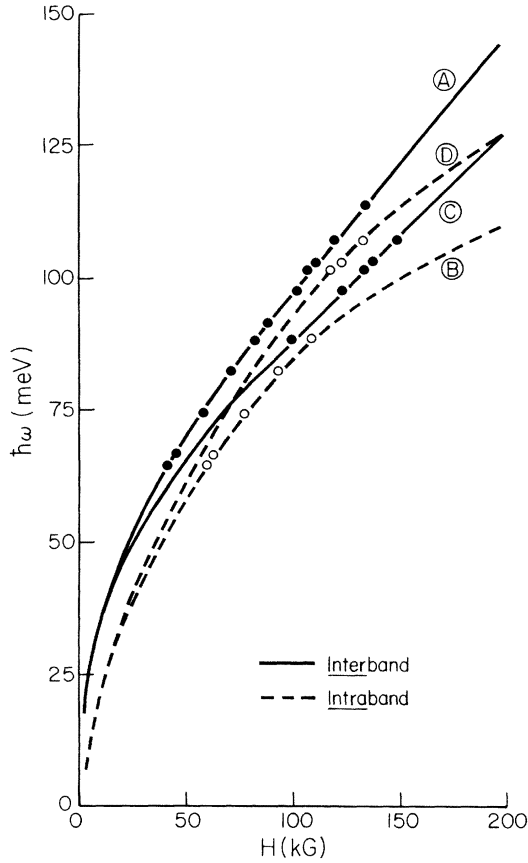


FIG. 10. Resonant photon energy versus magnetic field for the cluster of $j = 0$ transitions for the light binary electrons of bismuth at $T \sim 22.5$ K. The solid and dashed lines represent the calculated resonant positions of the interband and intraband transitions, respectively, and the circles show the experimental data. The transitions are labeled as indicated in the insert of Fig. 5. Of particular interest is the crossing of transitions (C) and (D) at about 75 and 200 kG.

dence of the $j = 1$ spin splitting, we expect that the (C) and (D) transitions will again cross; this occurs in Fig. 10 at $H \approx 200$ kG and $\hbar\omega \approx 128$ meV. Since $\hbar\omega \approx 128$ meV is close to the $10.6\text{-}\mu\text{m}$ CO_2 laser line, it may be possible to test this prediction experimentally. It may also be possible to test this prediction with $\text{Bi}_{1-x}\text{Sb}_x$ alloys, for which these effects should be observable at lower magnetic fields.

It is of interest to examine the H and ξ dependences of the velocity matrix elements associated with each of the four transitions (A), (B), (C), and (D), and these are shown in Figs. 11 and 12, respectively, using the same set of band parameters as in Figs. 8–10. In these figures, the velocity matrix element is expressed in units such that $|M|^2 = 1.0$ corresponds to approximately $25v_F^2$,

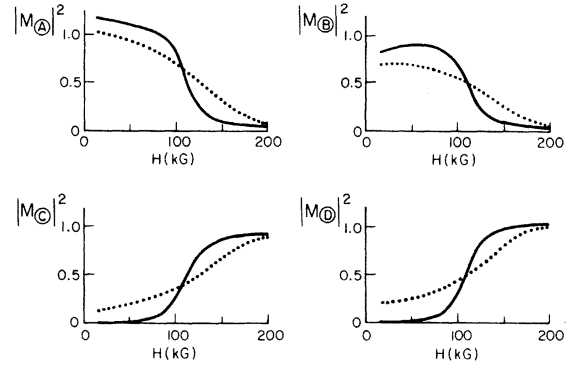


FIG. 11. Magnetic field dependence (\vec{H} parallel to the binary axis) of the square of the velocity matrix elements for $\xi = 0$ (solid curves) and $\xi = 1$ (dotted curves) for the four transitions shown in the insert to Fig. 5. Of particular interest is the magnetic-field-induced interchange of M_A with M_C , and M_B with M_D , as well as the magnetic field range over which this interchange occurs.

where v_F = Fermi velocity, and the curves have not been extended to $H = 0$ because in that limit nonparabolic effects introduce complicating features that are extraneous to our discussion. In Fig. 11 we note that for $\xi = 0$ (solid curves) there is an almost complete interchange between the transitions (A) and (B), which dominate at low H , to the transitions (C) and (D), which dominate at high H . This interchange occurs over a narrow range of H in the vicinity of 110 kG, corresponding to H_{min} in Fig. 2. We further observe that this interchange is more gradual for $\xi \neq 0$, as can be

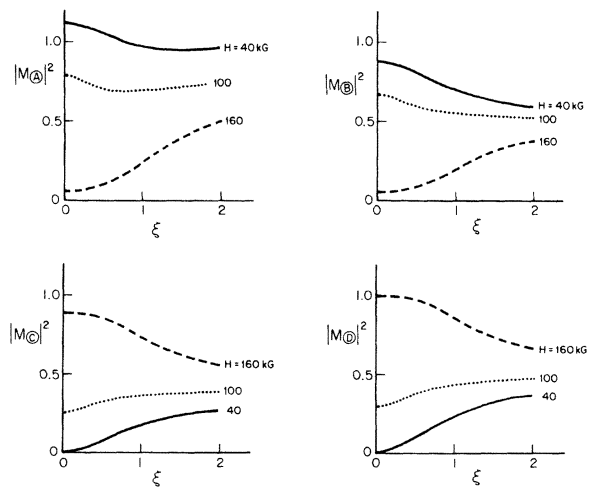


FIG. 12. ξ dependence of the square of the velocity matrix elements for the four transitions shown in the insert to Fig. 5 at $H = 40$ kG ($H \ll H_{\text{min}}$) (solid curve), 100 kG ($H \sim H_{\text{min}}$) (dotted curve), and 160 kG ($H \gg H_{\text{min}}$) (dashed curve). The magnetic-field-induced interchange of wave functions is most pronounced for small ξ values.

seen in the dotted curves of Fig. 11 drawn for $\xi = 1$, corresponding to $k_3 \approx 1.4k_F$ where $\hbar k_F$ is the Fermi momentum. This can be understood because all the unperturbed velocity matrix elements [Eqs. (21)] have finite magnitudes at $\xi \neq 0$. This point is demonstrated in more detail in Fig. 12 where each of the squared velocity matrix elements $|M_A|^2$, $|M_B|^2$, $|M_C|^2$, and $|M_D|^2$ given by Eq. (41) is plotted versus ξ in the low, intermediate, and high magnetic regimes.

V. DISCUSSION OF OTHER RELATED WORK

It is of interest to investigate the implications of the magnetic energy level model, which was developed to explain the magnetoreflexion experiments in the low-quantum-number limit, on other experiments. Of particular significance is the connection between the electron population in the $j=0$ conduction subband and the magnetic field dependence of the total carrier concentration and of the Fermi energy, since only modest magnetic fields are required to lift all other electron subbands above the Fermi energy (e.g., ~ 15 kG for the light binary electrons and ~ 25 kG for the heavy bisectrix electrons). The Fermi level is determined by the requirement

$$\sum_{i=1}^3 n_i = p, \quad (42)$$

where n_i denotes the electron concentration in pocket i , and p is the hole concentration of the hole pocket located at the T point in the Brillouin zone. For \vec{H} parallel to the binary axis, the electrons with heavy cyclotron effective masses have a very small density of states at high magnetic fields so that the total electron concentration is dominated by electrons with light cyclotron effective masses. Thus at sufficiently high magnetic fields where only the $j=0$ level is occupied, we have the approximate relation

$$n_i(j=0) \sim p, \quad (43)$$

where $n_i(j=0)$ is the total light electron carrier concentration from the various carrier pockets.

To study the magnetic field dependence of E_F and p , Shubnikov-de Haas measurements were made at high steady magnetic fields, in the regime where the resonant structures are associated with the passage of *hole* Landau levels through the Fermi level. Previous workers have reported Shubnikov-de Haas results for pure bismuth and for bismuth-antimony alloys in steady magnetic fields up to 80 kG and in pulsed fields up to 175 kG.²⁹⁻³² Our measurements were made in steady magnetic fields up to 220 kG on pure bismuth (\vec{H} parallel to the binary, bisectrix axes) and on $\text{Bi}_{1-x}\text{Sb}_x$ alloys (\vec{H} parallel to the binary axis and $x = 0.02, 0.03, 0.05$). A typical Shubnikov-de Haas

trace showing $\rho(H)$ and $\partial\rho(H)/\partial H$ is given in Fig. 13, where the hole and electron resonances are labeled, respectively, by the passage of the n th and j th magnetic subband through E_F . This figure clearly shows the power of the modulation technique to enhance the resonant structures which appear as small changes in $\rho(H)$ on a large background resistance.³³ A summary of the experimental results obtained for pure bismuth with \vec{H} parallel to the binary axis and \vec{H} parallel to the bisectrix axis is given in Table III. Also included in this table are the calculated values of the resonances, using a value of 38.7 meV for the zero-field band overlap for pure bismuth³⁴ (which is determined from the magnetic field position at which the $j=1$ electron level crosses the Fermi energy) and the band parameters for the electron $j=0$ magnetic subband, as given in Tables I and II. Since the band gap for the T point is large compared with the Landau-

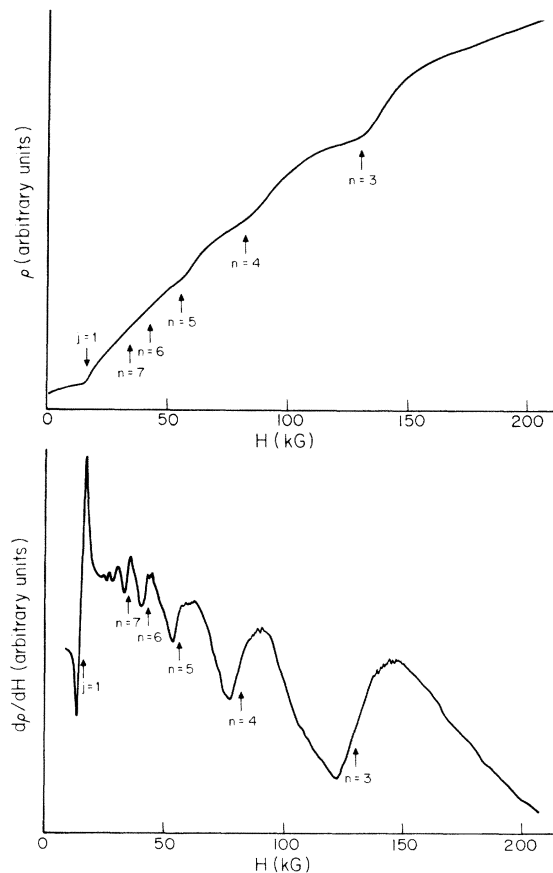


FIG. 13. Experimental trace of the Shubnikov-de Haas effect in bismuth for \vec{H} parallel to the binary axis at 4.2 K. The upper trace shows the transverse magnetic-field-dependent resistivity $\rho(H)$ and the lower trace shows its derivative $\partial\rho(H)/\partial H$. The magnetic fields at which the Landau levels cross the Fermi level are labeled by the Landau-level index j for electrons and n for holes.

TABLE III. Shubnikov-de Haas resonant magnetic fields for holes (in kG).

Landau-level index	Bismuth, \vec{H} parallel to the binary axis		Bismuth, \vec{H} parallel to the bisectrix axis		$\text{Bi}_{0.98}\text{Sb}_{0.02}$, \vec{H} parallel to the binary axis	
	Experiment	Theory	Experiment	Theory	Experiment	Theory
2	172.5	170.8
3	134.3	135.6	146.1	145.2	129.8	129.3
4	83.8	84.8	92.5	93.1	94.3	93.8
5	58.0	59.5	62.6	62.9	54.0	62.0
6	44.7	45.0	43.8	42.4	38.8	42.6
7	34.0	34.5	28.8	32.0
8	28.7	28.3	21.8	25.0

level separation in the hole band,³⁵ a simple parabolic band model has been assumed for the holes. Values for the band parameters for holes and heavy binary electrons were taken from Smith, Baraff, and Rowell.²⁹ The excellent agreement obtained between theory and experiment for the Shubnikov-de Haas data in Table III provides additional support for the validity of our model for the $j=0$ electron levels.

We also attempted an interpretation of our Shubnikov-de Haas experiments on the semimetallic $\text{Bi}_{1-x}\text{Sb}_x$ alloys using the same model for both holes and electrons as was used for pure bismuth. The hole effective masses for the $\text{Bi}_{1-x}\text{Sb}_x$ alloys with $x \leq 0.01$ have been reported to be the same as for pure bismuth, which is physically reasonable, because of the relatively larger T -point band gaps. Our results,¹⁰ however, suggest that for $x \geq 0.02$, the hole effective-mass parameters depend on x . For this reason, no quantitative interpretation could be given to the present Shubnikov-de Haas data for $x > 0.02$, with \vec{H} parallel to the binary axis. Both the experimental and calculated results for $x = 0.02$ are given in Table III. The parameters for the light binary electrons in this alloy were obtained from our magnetoreflexion experiments. In the absence of direct measurements, the parameters for the heavy binary electrons were scaled from the values of pure bismuth²⁹ using the ratio determined from the light binary electrons in bismuth and $\text{Bi}_{0.98}\text{Sb}_{0.02}$. The agreement between the experimental and calculated values of the resonant magnetic fields is not as good as in the case of pure bismuth, indicating the need for careful measurements of the effective-mass parameters for the $\text{Bi}_{1-x}\text{Sb}_x$ alloys before a critical assessment can be made of the validity of our model for the $j=0$ levels in this alloy system. Recent cyclotron resonance experiments³⁶ on $\text{Bi}_{1-x}\text{Sb}_x$ alloys for $x \leq 0.04$ indicate a nonlinear dependence of the electron effective masses on Sb concentration, in agreement with the present work.¹⁰ The need for careful measurements is also indicated by the dis-

crepancy between our determination of the overlap energy of 37.0 meV for $\text{Bi}_{0.98}\text{Sb}_{0.02}$ (from the analysis of the magnetic field position at which the $j=1$ electron level crosses the Fermi energy), compared with the previously determined value of 45 meV.³¹ We feel that our value is more accurate, since it results in an agreement between experimental and calculated data over a much wider range of H than the previous work,³¹ which was limited to 10 kG. Their findings of a highly nonlinear variation of the overlap energy with Sb concentration³¹ suggest a more complicated dependence of the hole effective-mass parameters than is used here. From our experimental Shubnikov-de Haas data for the three alloys studied here, we conclude that a detailed determination of the hole effective-mass parameters in this alloy system is feasible because the observed hole resonances for the alloy system are more clearly resolved than for the case of pure bismuth,¹⁰ in contrast with the situation for the electrons.

The magnetic field dependence of the Fermi energy E_F and electron carrier density corresponding to our interpretation of the magnetoreflexion data ($H \leq 150$ kG) and the Shubnikov-de Haas data for \vec{H} parallel to the binary axis ($H \leq 220$ kG) is shown in Fig. 14. The Fermi energy in this figure is measured with respect to the energy minimum at $\xi=0$ of the $j=0$ conduction level for the light electrons (solid curve) and for the heavier electrons (dashed curve). One should remember that this energy reference for E_F is magnetic-field dependent and different for each of the electron pockets and therefore distinct curves must be drawn in Fig. 14 for the light and heavy electrons. In this figure, the structure on the curves of $E_F(H)$ at very low fields is due to the passage of light electron Landau levels through the Fermi level, and for $H \geq 15$ kG, the oscillatory structure is due to hole and heavy electron Landau levels crossing the Fermi level. At $H=0$, E_F is the same for all three electron carrier pockets, but as a magnetic field is applied, for example along \vec{H} parallel to the

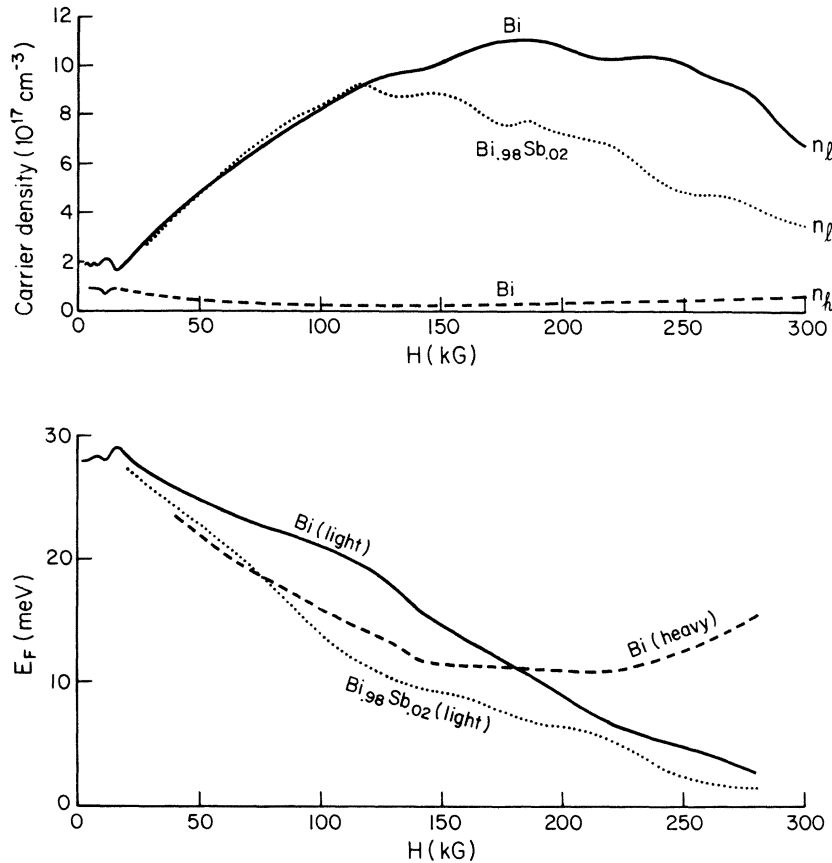


FIG. 14. Calculated magnetic field dependence of the electron carrier density and Fermi energy for pure bismuth and for the $\text{Bi}_{0.98}\text{Sb}_{0.02}$ alloy with \vec{H} parallel to the binary axis. The Fermi energies E_F are measured with respect to the energies of the $j=0$ conduction level at $\xi=0$ for the electrons with light (solid lines) and heavy (dashed lines) cyclotron effective masses. As $H \rightarrow 0$, the light electron carrier density for \vec{H} parallel to the axis becomes twice that for the heavy electrons, because in this orientation of \vec{H} , there are two equivalent electron ellipsoids with light cyclotron effective masses and a third electron ellipsoid with a heavy cyclotron effective mass.

binary axis, the electron pockets become nonequivalent; for this magnetic field orientation, there are two equivalent light electron pockets and a single heavy electron pocket, accounting for the 2:1 ratio of the light:heavy electron carrier concentration shown in Fig. 14 at low H .

For $H \geq 15$ kG, all the light electrons are in the $j=0$ level and their carrier density increases up to about 100 kG as shown in Fig. 14 because of the linear H dependence of the density of states. At yet higher fields $H > H_{\text{min}}$, the interband coupling between the $j=0$ levels becomes important and the extremum of the $j=0$ conduction level rises (see Fig. 2) so that there is a decrease in both the light electron carrier density and the energy difference between the Fermi level and the $j=0$ magnetic subband extremum. Figure 14 shows that in both the carrier density and E_F this effect due to the interband coupling between the two light electron $j=0$ levels occurs at lower H for the $\text{Bi}_{0.98}\text{Sb}_{0.02}$ alloy, and this is associated with the lower value of H_{min} in this alloy.

On the other hand, the H dependence of the heavy electron carrier density is quite different. For $H \leq 80$ kG, the $j=1$ magnetic subband for the heavy electrons loses carriers more rapidly than the

density of states is increased through its linear H dependence, and thus the carrier density for the heavy electrons decreases in this magnetic field regime. Above 80 kG, all the heavy electrons are in the $j=0$ magnetic subband and the linear increase in the density of states dominates, causing an increase in the heavy electron carrier density, as shown in Fig. 14. Nevertheless, the concentration of electrons with light cyclotron effective masses is dominant for $H \geq 15$ kG (see Fig. 14), and this has been verified by Alfvén wave propagation experiments up to 200 kG.³⁷

We observe in Fig. 14 that the decrease in carrier density for the light electrons at high fields is partly compensated by an increase in the carrier density for the heavy electrons, due to an increase in both the density of states and E_F for the heavy electrons. In this magnetic field regime, the hole carrier density is slowly decreasing.

Although we have plotted the magnetic field dependence of the electron carrier density and E_F up to 300 kG in Fig. 14, we must remember that our model is based on experimental data for $H \leq 200$ kG. These magnetic fields are too low to study the semimetal-semiconductor transition in pure bismuth,^{7-9,18} though in $\text{Bi}_{1-x}\text{Sb}_x$ alloys of suitable con-

centration x , it may be possible to observe such a transition and to develop a detailed model for the analysis of this effect, using an appropriate model for the two coupled $j=0$ levels. It should also be mentioned that the model presented here for the $j=0$ Landau levels should be applicable to the description of the magnetization of bismuth and $\text{Bi}_{1-x}\text{Sb}_x$ alloys at high fields.³⁸ Further work along these lines is currently in progress.

From this study we conclude that the model for the $j=0$ magnetic energy levels for the coupled L -point valence and conduction bands is consistent with both magnetoreflexion and Shubnikov-de Haas data for pure bismuth. The present work on the $\text{Bi}_{0.98}\text{Sb}_{0.02}$ alloy suggests that the same form of the

dispersion relation also applies to semimetallic $\text{Bi}_{1-x}\text{Sb}_x$ alloys for small x , though more careful experimental work on this alloy system will have to be performed before any definitive conclusions can be reached concerning the applicability of our model for the $j=0$ magnetic energy levels to these alloys.

ACKNOWLEDGMENTS

We wish to express our thanks to L. Rubin and the staff of the Francis Bitter National Magnet Laboratory for help with the experiments. We also thank Professor P. A. Wolff and Dr. G. F. Dresselhaus for valuable discussions.

*Based on a thesis submitted by one of the authors (M.P.V.) in partial fulfillment of the Ph.D. degree in Department of Electrical Engineering and Computer Science (MIT, 1975) (unpublished).

†Work supported by the NSF.

‡Work supported in part by the Instituto Venezolano de Investigaciones Científicas (IVIC); present address: IVIC, Caracas, Venezuela.

§Visiting Scientist: Francis Bitter National Magnet Laboratory, MIT, Cambridge, Mass., supported by the NSF.

¶Supported by Fundação de Amparo à Pesquisa do Estado de São Paulo (FAPESP), Brazil. Present address: University of São Paulo, Brazil.

¹M. P. Vecchi and M. S. Dresselhaus, Phys. Rev. B **9**, 3257 (1974). In this reference Q is denoted by \sqrt{P} .

²M. H. Cohen and E. I. Blount, Philos. Mag. **5**, 115 (1960).

³R. N. Brown, J. G. Mavroides, and B. Lax, Phys. Rev. **129**, 2055 (1963).

⁴P. A. Wolff, J. Phys. Chem. Solids **25**, 1057 (1964).

⁵M. Maltz and M. S. Dresselhaus, Phys. Rev. B **2**, 2877 (1970).

⁶G. A. Baraff, Phys. Rev. **137**, A842 (1965).

⁷N. B. Brandt, E. A. Svistova, and Yu. G. Kashirskii, Zh. Eksp. Teor. Fiz. Pis'ma. Red. **9**, 232 (1969)

[Sov. Phys.-JETP Lett. **9**, 136 (1969)]; N. B. Brandt and E. A. Svistova, J. Low Temp. Phys. **2**, 1 (1970).

⁸N. B. Brandt, E. A. Svistova, Yu. G. Kashirskii, and L. B. Lyn'ko, Zh. Eksp. Teor. Fiz. Pis'ma Red. **7**, 441 (1968) [Soviet Phys.-JETP Lett. **7**, 347 (1968)].

⁹N. B. Brandt, E. A. Svistova and R. G. Valeev, Zh. Eksp. Teor. Fiz. **55**, 469 (1968) [Soviet Phys.-JETP **28**, 245 (1969)].

¹⁰M. P. Vecchi, Ph.D. thesis (MIT, 1975) (unpublished). In this reference Q is denoted by \sqrt{P} .

¹¹A more complete description of the experimental set-up is given in Ref. 10.

¹²The optical system was kindly made available to us by Dr. R. L. Aggarwal of the Francis Bitter National Magnet Laboratory.

¹³The bismuth crystals were kindly supplied to us by E. J. Alexander of the Francis Bitter National Magnet Laboratory.

¹⁴The various bismuth-antimony alloy samples used in

the present work were kindly supplied to us by Dr. J. G. Mavroides of the MIT Lincoln Laboratory.

¹⁵M. S. Maltz, Ph.D. thesis (MIT, 1968) (unpublished).

¹⁶B. McCombe and G. Seidel, Phys. Rev. **155**, 633 (1966).

¹⁷To make this comparison meaningful, the coefficients are normalized by

$$\sum_{l'=1}^2 |a_{ll'}|^2 = 1, l=1, 2.$$

In the (6×6) secular equation, the coupling coefficients $a_{ll'}$ between the $j=0$ and $j=1$ levels are very small, and therefore this normalization condition is appropriate.

¹⁸M. P. Vecchi, J. R. Pereira, and M. S. Dresselhaus, *Proceedings of the International Conference on the Physics of Semiconductors, Stuttgart, 1974*, edited by M. H. Pilkuhn (Taubner, Stuttgart, 1974), p. 1181. In this reference Q is denoted by \sqrt{P} .

¹⁹M. P. Vecchi and M. S. Dresselhaus, Phys. Rev. B **10**, 771 (1974). In this reference Q is denoted by \sqrt{P} .

²⁰E. J. Tichovol'sky and J. G. Mavroides, Solid State Commun. **7**, 927 (1969).

²¹E. J. Tichovol'sky, M. S. thesis (MIT, 1969) (unpublished).

²²M. S. Dresselhaus and G. Dresselhaus, Phys. Rev. **125**, 499 (1962).

²³Although the experimental spectra are taken at ~ 22.5 K, the temperature dependence of the Fermi functions in Eq. (36) was neglected.

²⁴C. Nanney, Phys. Rev. **129**, 109 (1963).

²⁵R. D. Brown III, Phys. Rev. B **2**, 928 (1970).

²⁶V. Strom, A. Kamgar, and J. F. Koch, Phys. Rev. B **7**, 2435 (1973).

²⁷R. L. Hartman, Phys. Rev. **181**, 1070 (1969).

²⁸H. D. Drew and U. Strom, Phys. Rev. Lett. **25**, 1755 (1970).

²⁹G. E. Smith, G. A. Baraff, and J. M. Rowell, Phys. Rev. **135**, A1118 (1964).

³⁰H. T. Chu and Y. Kao, Phys. Rev. B **1**, 2369 (1970).

³¹P. W. Chao, H. T. Chu, and Y. H. Kao, Phys. Rev. B **9**, 4030 (1974).

³²J. Vuillemin, IBM J. Res. Dev. **8**, 232 (1964).

³³The experimental resonant points are taken as the mid-point between the maximum and minimum of the resonance in dp/dH . Since the derivative is a sensitive func-

tion of H , the error introduced by this method for the determination of the resonant position is small.

³⁴This value is in good agreement with previous work (Refs. 29 and 31). The band overlap only has meaning at $H = 0$, because at higher magnetic fields the energy difference between the Fermi energy and the band extremum is different for the pockets with light and heavy cyclotron effective masses.

³⁵B. T. Smith and A. J. Sievers, *Phys. Lett. A* 51, 273 (1975).

³⁶R. Herrmann, W. Braune, and G. Kuka, *Phys. Status Solidi B* 68, 233 (1975).

³⁷S. Takano and H. Kawamura, *J. Phys. Soc. Jpn.* 28, 348 (1970).

³⁸J. W. McClure and D. Shoenberg, *J. Low Temp. Phys.* 22, 233 (1976).